Universität Karlsruhe (TH)
Institut für Baustatik

Coupling of 2D– and 3D–Composite Shell Elements in Linear and Nonlinear Applications

F. Gruttmann, W. Wagner

Mitteilung 3(1996)

Universität Karlsruhe (TH)
Institut für Baustatik

Coupling of 2D– and 3D–Composite Shell Elements in Linear and Nonlinear Applications

F. Gruttmann, W. Wagner

Mitteilung 3(1996)

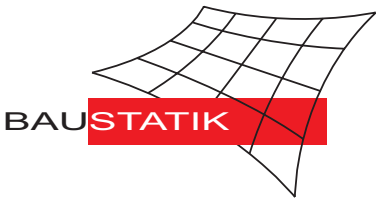

Prof. Dr.–Ing. W. Wagner
Institut für Baustatik
Universität Karlsruhe
Postfach 6980
76128 Karlsruhe

Telefon: (0721) 608–2280
Telefax: (0721) 608–6015
E–mail: bs@.uni-karlsruhe.de
Internet: http://www.bs.uni-karlsruhe.de

Coupling of 2D– and 3D–Composite Shell Elements in Linear and Nonlinear Applications

F. Gruttmann and **W. Wagner**
Institut für Baustatik, Universität Karlsruhe,
Kaiserstraße 12, 76131 Karlsruhe, Germany

Contents

Abstract

A numerical model for the nonlinear analysis of laminates is presented. The developed element is based on piecewise polynomial interpolation in thickness direction. Although the total number of degrees of freedom is comparable to a discretization with 3–D brick elements this approach provides several advantages, e.g. a simple mesh generation due to a 2D–type data structure and a better bending behaviour. The developed isoparametric quadrilateral finite element allows to predict the complete stress state. Furthermore a transition element is presented which is capable to couple the developed element with 5–parameter shell elements. Several linear and nonlinear examples are presented to illustrate the performance of the developed numerical model.

1 Introduction

The application of composite materials in shell–like light weight structures demands new design requirements. These shells usually consist of thin laminates which are treated as a stack of bonded plies. Due to the varying fiber orientations and the anisotropy of the material each ply tries to behave independently of the other plies. This leads to a complicated three–dimensional stress state e.g. along free edges, cutouts, rivet holes etc.. The stress state, especially tension stresses in thickness direction and shear stresses, may lead to delamination between adjacent layers. Since there are many papers on the topic of composite shells, only a few representative results are mentioned in the following. Detailed surveys are given in refs. [1] , [2].

Shear deformation models are variants of the Reissner–Mindlin theory which was originally proposed for homogeneous isotropic plates. A generalization of the shear–deformable theory for composite materials leads to the classical laminate theory where coupling of bending and stretching occurs. These models do not account for continuity of the shear stress components acting on laminar interfaces. The performance of this first–order shear–deformation model depends on the factors used for adjusting the transverse shear stiffness, see e.g. refs. [3] , [4] .

Cubic polynomials in thickness direction are used to interpolate the displacements in third–order shear–deformation models [5]. In general these models do not fulfill continuity of the stresses across the interfaces. Only with special Hermite cubic shape functions continuity of the interlaminar shear stresses can be achieved [6].

In discrete–layer models the shape of the displacement field through the thickness is interpolated by piecewise linear functions (multi–director theory). The number of field equations and edge boundary conditions depends on the number of layers. Each layer is considered as a homogeneous shell with constant material properties.

For all these models closed form solutions are available only in special cases with simple geometry and boundary conditions, see e.g. ref. [7]. In many cases the finite element method is used to compute numerical results. Finite elements for linear composite plate and shells have been described in many papers, see e.g. refs. [8] - [17], and with nonlinear applications e.g. in [18] - [31].

The objective of this paper is to develop a geometrical nonlinear 2–D, displacement–based finite element model which is capable to predict edge stresses in laminates emanating from the anisotropy of the material. We apply piecewise polynomial functions up to third order to interpolate the displacements in thickness direction. This shape is independent of the FE–interpolation in the shell middle surface, see ref. [17]. Within a nonlinear formulation the theory accounts for all six strain components. Each layer has constant material properties and is treated as a homogeneous shell.

The second part is concerned with the finite element formulation for quadrilaterals. The initial configuration is described using an arbitrary reference surface and associated normal vector. Within the so–called isoparametric approach we apply bilinear shape functions to interpolate the reference surface and the displacement vector at the layer points. We present the discrete weak form of equilibrium and derive analytically the tangent stiffness matrix.

Large portions of composite structures are characterized by plane stress state and straight director vector in the current configuration. These are typical assumptions for shell elements based on standard shell theories. We develop a transition element which is capable to connect the generalized finite element with standard shell elements with five degrees of freedom (three displacements and two rotations). Composites behave very sensitive to any constraints within the transition area. Numerical investigations show that especially for a membrane stress state constraints concerning the strain in thickness direction lead to local spurious effects. Thus the transition conditions have to be chosen in a proper way to obtain reasonable results. We present linear and nonlinear examples which show the effectivity of the proposed model.

2 Kinematic, Weak Form and Material Law

The variational formulation of the boundary value problem is presented. Within a material formulation the kinematic of a laminate is discussed. Furthermore the static field equations, the associated weak formulation and the orthotropic material law are given.

In the definitions and relations that follow Greek subscripts and superscripts refer to covariant and contravariant surface tensor components, respectively. The summation convention applies to each repeated pair of indices. Commas are used to denote partial differentiation based on the geometry of the arbitrary reference surface Ω. The shell consists of N **numerical** layers with thickness ${}^{i}h$. The numerical layers are not necessarily identical with the n **actual** layers of thickness ${}^{j}h$. Thus each actual layer can be subdivided into several sublayers or viceversa several layers can be summarized to an equivalent numerical layer (see Fig. 1).

The position vector $\mathbf{X}_0$ is labeled with convective coordinates Θ^α. An orthonormal basis system $\mathbf{t}_k(\Theta^\alpha)$ is attached to this surface where $\mathbf{t}_3$ is a normal vector and Θ^3 the coordinate in thickness direction. The transformations between the different base systems are given by

$$\mathbf{t}_k(\Theta^\alpha) = \mathbf{R}_0(\Theta^\alpha)\,\mathbf{e}_k \tag{1}$$

where $\mathbf{R}_0$ is a proper orthogonal tensor. This leads to a convenient representation of the orthotropic material law.

The kinematic of the shell is based on the assumption of a multiplicative decomposition of the displacement field in shell space with independent functions for the shape in thickness direction and functions defined on the reference surface of the shell.

Then the position vectors of the reference and the current configuration are given by (see Fig. 2)

$$\begin{aligned} \mathbf{X}(\Theta^\alpha,\Theta^3) &= \mathbf{X}_0(\Theta^\alpha) + \Theta^3\,\mathbf{t}_3(\Theta^\alpha) \qquad -\frac{h}{2} \le \Theta^3 \le \frac{h}{2} \\ \mathbf{x}(\Theta^\alpha,\Theta^3) &= \mathbf{X}(\Theta^\alpha,\Theta^3) + \mathbf{u}(\Theta^\alpha,\Theta^3) \end{aligned} \tag{2}$$

where for layer i the displacement vector is interpolated through the thickness

$$\begin{aligned} \mathbf{u}(\Theta^\alpha, \Theta^3) &= \sum_{l=1}^{m} {}^i\phi_l(\Theta^3)\, {}^i\bar{\mathbf{u}}_l(\Theta^\alpha) = {}^i\mathbf{\Phi}(\Theta^3)\, {}^i\bar{\mathbf{u}}(\Theta^\alpha) \\ {}^i\bar{\mathbf{u}}(\Theta^\alpha) &= [{}^i\bar{\mathbf{u}}_1, {}^i\bar{\mathbf{u}}_2, \quad \ldots \quad, {}^i\bar{\mathbf{u}}_m]^T \quad (2 \le m \le 4)\,. \end{aligned} \tag{3}$$

The shape functions ${}^i\phi_l$ are written in a matrix with hierarchical shape functions

$$\begin{aligned} {}^i\mathbf{\Phi} &= [{}^i\phi_1\mathbf{1}, {}^i\phi_2\mathbf{1}, \quad \ldots \quad, {}^i\phi_m\mathbf{1}] \\ {}^i\phi_1({}^i\zeta) &= \frac{1}{2}(1 - {}^i\zeta) \qquad {}^i\zeta = 2\,\Theta^3/{}^ih \\ {}^i\phi_2({}^i\zeta) &= \frac{1}{2}(1 + {}^i\zeta) \\ {}^i\phi_3({}^i\zeta) &= 1 - {}^i\zeta^2 \\ {}^i\phi_4({}^i\zeta) &= (1 - {}^i\zeta^2){}^i\zeta \end{aligned} \tag{4}$$

Thus up to third order polynomial functions are used to describe the shape of the deformed cross sections (see Fig. 3). For example a layerwise linear shape of the deformed cross section through the thickness is obtained using ${}^i\phi_1$ and ${}^i\phi_2$.

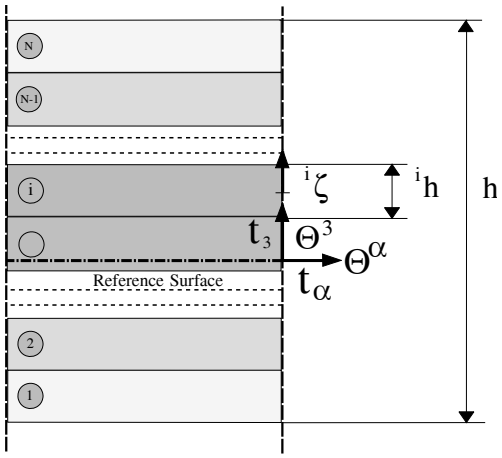

Figure 1: Subdivision of the laminate into N numerical layers, notation

The governing static field equations and boundary conditions of the three–dimensional theory are

$$\begin{aligned} &\mathrm{Div}\,(\mathbf{F}\,\mathbf{S}) + \rho_0\mathbf{b} = \mathbf{0} \\ &\mathbf{S} = \mathbf{S}^T \end{aligned} \quad \text{in} \quad B \qquad \begin{aligned} (\mathbf{F}\,\mathbf{S})\,\mathbf{n}_0 &= \hat{\mathbf{p}} \quad \text{on} \quad \partial B_\sigma \\ \mathbf{u} &= \hat{\mathbf{u}} \quad \text{on} \quad \partial B_u \end{aligned} \tag{5}$$

Here $\mathbf{S}$ and $\mathbf{F}$ are the Second Piola–Kirchhoff stress tensor $\mathbf{S} = S^{kl}\mathbf{G}_k \otimes \mathbf{G}_l$ and deformation gradient $\mathbf{F} = F^k_m \mathbf{G}_k \otimes \mathbf{G}^m$, respectively. In a standard manner the covariant base vectors are introduced as $\mathbf{G}_i = \partial\mathbf{X}/\partial\Theta^i$, whereas the dual base vectors $\mathbf{G}^i$ are defined by $\mathbf{G}_i \cdot \mathbf{G}^j = \delta^j_i$. In (5) $\mathbf{n}_0$ denotes the outward normal vector along the top and bottom surface ∂B_σ with applied loads $\hat{\mathbf{p}} = \hat{p}^k\,\mathbf{e}_k$. The body forces $\rho_0\mathbf{b}$ are neglected in the following equations.

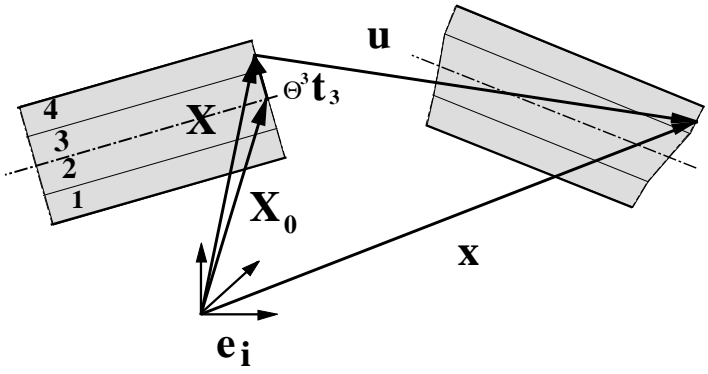

Figure 2: Initial and current configuration of a laminated shell

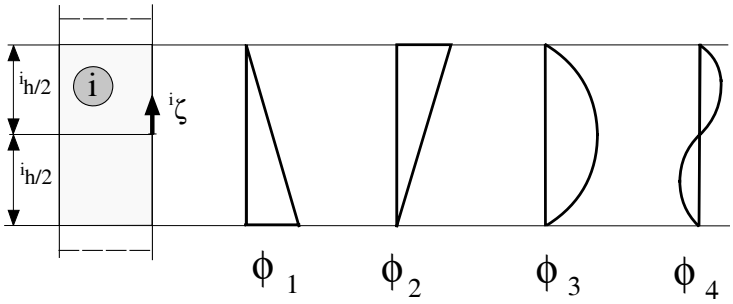

Figure 3: Hierarchical shape functions in thickness direction for numerical layer i

The associated weak formulation in a material description is obtained by weighting the field equations with test functions $\delta\mathbf{u}$ which yields after some algebraic manipulations

$$\mathbf{g}(\mathbf{u},\delta\mathbf{u}) = \int_{(\Omega)} [\int_{(\Theta^3)} S^{kl}\,\delta E_{kl}\,J d\Theta^3]\,d\Theta^2 d\Theta^1 - \int_{(\Omega_\sigma)} \widehat{p}^k\,\delta u_k\,d\Omega_\sigma = 0\,. \tag{6}$$

with $J = (\mathbf{X}_{,1}\times\mathbf{X}_{,2})\cdot\mathbf{X}_{,3}$. Note that integration in (6) has to be performed considering the different material parameters or fiber angles through the thickness. The components of the Green-Lagrangian strain tensor $\mathbf{E} = E_{kl}\,\mathbf{G}^k\otimes\mathbf{G}^l$ and the associated variation yields

$$\begin{aligned} E_{kl} &= \tfrac{1}{2}(\mathbf{x}_{,k}\cdot\mathbf{x}_{,l} - \mathbf{X}_{,k}\cdot\mathbf{X}_{,l})\\ \delta E_{kl} &= \tfrac{1}{2}(\delta\mathbf{x}_{,k}\cdot\mathbf{x}_{,l} + \delta\mathbf{x}_{,l}\cdot\mathbf{x}_{,k})\,. \end{aligned} \tag{7}$$

Furthermore we need to express the linearization of the weak form. With conservative external loads one obtains

$$D\mathbf{g}(\mathbf{u},\delta\mathbf{u})\cdot\Delta\mathbf{u} = \int_{(\Omega)} [\int_{(\Theta^3)} (\delta E_{kl} C^{klmn}\Delta E^{mn} + S^{kl}\Delta\delta E_{kl})\,J d\Theta^3]\,d\Omega \tag{8}$$

with the linearized virtual strains

$$\Delta\delta E_{kl} = \tfrac{1}{2}(\delta\mathbf{x}_{,k}\cdot\Delta\mathbf{x}_{,l} + \delta\mathbf{x}_{,l}\cdot\Delta\mathbf{x}_{,k})\,. \tag{9}$$

Besides the kinematical relations and the equilibrium equations we have to formulate a constitutive law to determine the deformations of the shell. Each ply is considered as a

homogeneous orthotropic medium, where the axes of orthotropy coincide with the material principal axes.

Hence the stresses of the actual layer j are given with the orthotropic material law

$$ {}^{j}S^{kl} = {}^{j}C^{klmn\,j}E_{mn}\,. \tag{10} $$

The components expressed in matrix notation refer to an orthonormal coordinate system which is a local fiber oriented basis. The material matrix has to be transformed to a global fiber independent basis system, for more details see e.g. [30]

$$ \begin{aligned} {}^{j}\mathbf{S} &= {}^{j}\mathbf{C}\,{}^{j}\mathbf{E} \\ {}^{j}\mathbf{S} &= [S^{11}\,, S^{22}\,, S^{33}\,, S^{12}\,, S^{13}\,, S^{23}]^{T} \\ {}^{j}\mathbf{E} &= [E_{11}\,, E_{22}\,, E_{33}\,, 2E_{12}\,, 2E_{13}\,, 2E_{23}]^{T} \end{aligned} \tag{11} $$

with the constitutive matrix

$$ {}^{j}\mathbf{C} = \begin{bmatrix} Q_{11} & Q_{12} & Q_{13} & Q_{14} & 0 & 0 \\ Q_{21} & Q_{22} & Q_{23} & Q_{24} & 0 & 0 \\ Q_{31} & Q_{32} & Q_{33} & Q_{34} & 0 & 0 \\ Q_{41} & Q_{42} & Q_{43} & Q_{44} & 0 & 0 \\ 0 & 0 & 0 & 0 & Q_{55} & Q_{56} \\ 0 & 0 & 0 & 0 & Q_{65} & Q_{66} \end{bmatrix} \tag{12} $$

The components Q_{ij} are functions of the material parameters $E_1, E_2, \nu, G_{12}, G_{23}$ of layer j and of the fiber angle ${}^{j}\varphi$. The moduli E_1 and E_2 are the stiffness ratios parallel and perpendicular to the fiber direction, respectively. The fiber angle is defined in our calculations as angle between fiber direction and basis vector $\mathbf{t}_1$.

We restrict ourselves to small strains thus transformations between different stress tensors are neglected and material parameters of the linear theory can be used.

3 Finite Element Formulation

In this section the finite element formulation for quadrilaterals is developed. The initial geometry is approximated using standard bilinear shape functions. Due to the above presented variational formulation only C^0–continuity for the displacements at the element boundaries is necessary. Furthermore the transverse shear strains are interpolated in such a way that shear locking can be avoided. In the following we denote our shell–formulation as **'3D–shell'** whereas we call an element based on a 5–parameter theory a **'2D–shell'**.

The shell surface is approximated by a finite element discretization of the form

$$ \Omega^{h} = \mathop{\mathsf{A}}_{e=1}^{n_{elm}} \Omega_e\,, \tag{13} $$

where n_{elm} is the number of finite elements in the discretization, and Ω_e denotes a typical element.

Within an element Ω_e, the position vector $\mathbf{X}$ of the reference configuration is interpolated by

$$\begin{aligned} \mathbf{X} &= \sum_{K=1}^{4} N_K(\xi,\eta)\,\mathbf{X}_K \\ \mathbf{X}_K &= \mathbf{X}_{0K} + \Theta^3\,\mathbf{t}_{3K} \end{aligned} \tag{14}$$

Here Θ^3 takes the value of integration points in thickness direction. The functions $N_K(\xi,\eta)$ are the standard bilinear element shape functions. The normal vectors $\mathbf{t}_{3K}$ are computed within the mesh generation and have to be unique at the nodes.

Using (14) we compute an orthonormal basis system at the integration points.

$$\begin{aligned} \mathbf{t}_1 &= \mathbf{G}_1/\|\mathbf{G}_1\| \\ \mathbf{t}_3 &= (\mathbf{G}_1\times\mathbf{G}_2)/\|\mathbf{G}_1\times\mathbf{G}_2\| \\ \mathbf{t}_2 &= \mathbf{t}_3\times\mathbf{t}_1 \end{aligned} \tag{15}$$

where the convected system is obtained by partial derivatives

$$\begin{aligned} \mathbf{G}_1 &= \partial\mathbf{X}/\partial\xi, \\ \mathbf{G}_2 &= \partial\mathbf{X}/\partial\eta\,. \end{aligned} \tag{16}$$

The advantage of the orthogonal system (15) compared with a convected system is that no further transformations of the material law are necessary.

Then the Jacobian transformation matrix follows from

$$\mathbf{J} = \begin{bmatrix} \mathbf{G}_1\cdot\mathbf{t}_1 & \mathbf{G}_1\cdot\mathbf{t}_2 \\ \mathbf{G}_2\cdot\mathbf{t}_1 & \mathbf{G}_2\cdot\mathbf{t}_2 \end{bmatrix}. \tag{17}$$

This matrix is used to obtain the shape function derivatives with respect to the local orthonormal coordinates.

Furthermore the displacement vector $\mathbf{u} = u^l\mathbf{e}_l$ is approximated using (3)

$$\mathbf{u} = \sum_{K=1}^{4} N_K(\xi,\eta)^i\mathbf{\Phi}\,\mathbf{v}_K\,. \tag{18}$$

Here the nodal displacement vector $\mathbf{v}_K$ consists of $ndf = 3(N+1)+3N(m-2)$ unknowns.

To avoid shear locking the transverse shear strains $\boldsymbol{\gamma} = E_{\xi 3}\mathbf{G}^1 + E_{\eta 3}\mathbf{G}^2$ are independently interpolated (see ref. [40]):

$$\begin{aligned} 2E_{\xi 3} &= \tfrac{1}{2}[(1-\eta)\gamma_B + (1+\eta)\gamma_D] \\ 2E_{\eta 3} &= \tfrac{1}{2}[(1-\xi)\gamma_A + (1+\xi)\gamma_C]\,. \end{aligned} \tag{19}$$

The shear strains γ_M at the midside nodes $M = A,B,C,D$ of a four–node element (see Fig. 4) are deduced with $(7)_1$ for certain coordinates Θ^3

$$\gamma_\alpha = \mathbf{x}_{,\alpha}\cdot\mathbf{x}_{,3} - \mathbf{X}_{,\alpha}\cdot\mathbf{X}_{,3}\,. \tag{20}$$

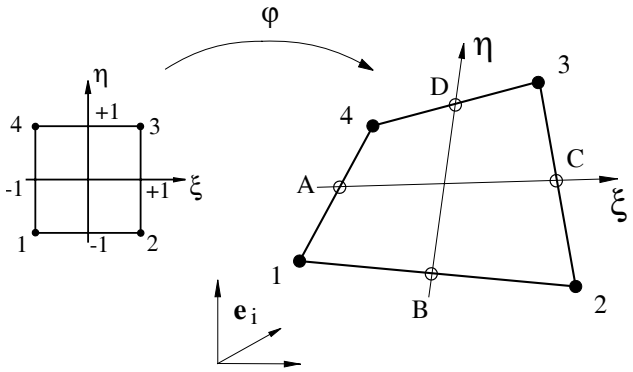

Figure 4: Quadrilateral shell element

Inserting the preliminary interpolations into the virtual work expression the FE–equations of the weak form are obtained

$$g^e(\mathbf{v},\delta\mathbf{v}) = \sum_{K=1}^{nel} \delta\mathbf{v}_K^T \left\{ \int_{(\Omega_e)} [\sum_{j=1}^{n} \int_{(\Theta^3)} \mathbf{B}_K^T \mathbf{S} J \frac{{}^j h}{2} d^j\zeta]\, d\Omega_e - \sum_{l=1}^{2} \int_{(\Omega_{e\sigma})} N_K \hat{\mathbf{p}}_l \bar{J}_l \, d\Omega_{e\sigma} \right\} = 0\,. \tag{21}$$

Here $\bar{J}_l$ denotes the surface element of the top and bottom surface $\Omega_{e\sigma}$ with applied loads $\hat{\mathbf{p}}_l$. The stress vector $\mathbf{S}$ is obtained via the constitutive relation and matrix $\mathbf{B}_K$ is specified in detail in appendix A1.

The solution of the nonlinear algebraic equation (21) is iteratively computed by Newton's method. For this purpose the tangent stiffness is derived by applying the directional derivative to $\mathbf{g}$

$$\begin{aligned} D\mathbf{g}^e(\mathbf{v},\delta\mathbf{v})\Delta\mathbf{v} &= \sum_{K=1}^{nel}\sum_{L=1}^{nel} \delta\mathbf{v}_K^T \mathbf{K}_{TKL}^e \Delta\mathbf{v}_L \\ \mathbf{K}_{TKL}^e &= \int_{(\Omega_e)} \sum_{j=1}^{n} \int_{(\Theta^3)} (\mathbf{B}_K^T {}^j\mathbf{C}\, \mathbf{B}_L + {}^j\mathbf{G}_{KL})\, J \frac{{}^j h}{2} d^j\zeta \, d\Omega_e \end{aligned} \tag{22}$$

Here $\mathbf{K}_{TKL}^e$ denotes the tangential stiffness matrix for nodes K and L of the element e. The matrix ${}^j\mathbf{G}_{KL}$ follows from the discretization of the linearized virtual strains (9) and is given in appendix A2.

The derivation of the exact linearization is essential for the solution process of the nonlinear FE–equations. The vectors and matrices (21), (22) are integrated using Gauss quadrature with a 2×2 integration within the shell surface. For each layer the numerical integration through the thickness depends on the chosen polynomial degree, e.g. two integration points for linear and three and four for quadratic and cubic interpolation, respectively.

4 Transition Element

Usually large portions of composite structures are characterized by plane stress state and straight director vector in the current configuration. These are typical assumptions for shell elements based on standard shell theories. Coupling of 2D–shell elements with 3D–brick elements has been considered for linear elastic isotropic material behaviour e.g. in Stein, Rust, Ohnimus [37]. In this section we present a transition element which is capable to connect the developed finite element with standard shell elements with five degrees of freedom (three displacements and two rotational degrees of freedom).

As constraints at the intersection line we introduce two conditions:

(i) The cross section of the current configuration is a plane (no warping)

(ii) Layerwise constant thickness stretches
(plane stress state is approximately fulfilled within the 3d–weak form) .

Numerical investigations show that for laminated plies the assumption of inextensibility in thickness direction leads to a completely wrong stress distribution in the vicinity of the transition edges. Furthermore the computations show that the assumption of constant strain E_{33} through the total thickness is not sufficient. Therefore we assume **layerwise** constant strains in thickness direction.

Within a transition element the interpolation of the displacement vector has to be modified according to eq. (18)

$$\delta\mathbf{u} \;=\; \sum_{K=1}^{4} N_K(\xi,\eta)\tilde{\mathbf{\Phi}}_K\,\delta\mathbf{v}_K\,. \tag{23}$$

The matrix of the shape functions $\tilde{\mathbf{\Phi}}_K$ describes the interpolation in thickness direction where at the transition nodes K

$$\begin{aligned} \tilde{\mathbf{\Phi}}_K &= [\phi_1\mathbf{1},\phi_2\mathbf{1},\cdots,\phi_2\mathbf{1}] \\ \phi_1 &= 1 \\ \phi_2 &= \Theta^3\,. \end{aligned} \tag{24}$$

The vector of virtual nodal displacements at the transition nodes reads

$$\delta\mathbf{v}_K \;=\; [\delta\mathbf{u}_0,\delta^1\mathbf{d},\cdots,\delta^N\mathbf{d}]_K \tag{25}$$

Here $\mathbf{u}_0$ and ${}^i\mathbf{d}$ denote the displacement vector of the reference surface and director vector of layer i, respectively.

We apply a multiplicative split of the director vector ${}^i\mathbf{d}_K$ in a rotation and stretch in thickness direction ${}^i\lambda$ for each numerical layer $i\,(1\le i\le N)$.

$${}^i\mathbf{d}_K = {}^i\lambda_K\,\mathbf{a}_{3K} \qquad \|\mathbf{a}_{3K}\| = 1 \tag{26}$$

The variation of ${}^i\mathbf{d}_K$ is required and yields with logarithmic stretches $\mu=\ln\lambda$ and two local rotations β_α

$$\begin{aligned} \delta^i\mathbf{d}_K &= \delta^i\lambda_K\,\mathbf{a}_{3K} + {}^i\lambda_K\,\delta\mathbf{a}_{3K} \\ \delta\mathbf{a}_{3K} &= \delta\beta_{1K}\mathbf{a}_{1K} + \delta\beta_{2K}\mathbf{a}_{2K} \\ \delta^i\lambda_K &= {}^i\lambda_K\,\delta^i\mu_K\,. \end{aligned} \tag{27}$$

The associated matrix representation yields

$$\delta^i \mathbf{d}_K = {}^i\lambda_K \, \mathbf{T}_K \, \delta\boldsymbol{\beta}_K + {}^i\lambda_K \, \mathbf{a}_{3K} \, \delta^i\mu_K \tag{28}$$

where

$$\begin{aligned} \delta\boldsymbol{\beta}_K &= [\delta\beta_1, \delta\beta_2]_K^T \\ \mathbf{T}_K &= [\mathbf{a}_1, \mathbf{a}_2]_K \,. \end{aligned} \tag{29}$$

We emphasize that the decomposition is only performed at the transition nodes. The rotation matrix $\boldsymbol{\Lambda}_K = [\mathbf{a}_1, \mathbf{a}_2, \mathbf{a}_3]_K$ is obtained by a multiplicative update procedure within the Newton iteration process as described in ref. [36]. In case of moderate rotations the update drops out and the base vectors of the initial configuration $\mathbf{a}_{iK} = \mathbf{t}_{iK}$ are used in (28). We apply the same rotation matrix $\boldsymbol{\Lambda}_K$ for all layers, which coincides with assumption (i).

Inserting transformation (28) into (23) one obtains modified functions ${}^i\tilde{\boldsymbol{\Phi}}$.

$$\delta\mathbf{u} = \sum_{K=1}^{4} N_K(\xi,\eta) \, {}^i\tilde{\boldsymbol{\Phi}}_K \, \delta\mathbf{v}_K \tag{30}$$

where

$$\begin{aligned} {}^i\tilde{\boldsymbol{\Phi}}_K &= [\tilde{\boldsymbol{\Phi}}_{AK}, \tilde{\boldsymbol{\Phi}}_{BK}] \\ {}^i\tilde{\boldsymbol{\Phi}}_{AK} &= [\phi_1 \mathbf{1}, \phi_2 \, {}^i\lambda \mathbf{T}_K] \\ {}^i\tilde{\boldsymbol{\Phi}}_{BK} &= [\phi_2 \, {}^i\lambda \mathbf{a}_{3K}] \\ \delta\mathbf{v}_K &= [\delta\mathbf{u}_0, \delta\boldsymbol{\beta}, \cdots, \delta \, {}^i\mu, \cdots]_K \,. \end{aligned} \tag{31}$$

When computing the matrices $\mathbf{B}_K$ which are defined in appendix A1 one has to consider the following cases:

$$\begin{aligned} \mathbf{B}_{AK} &= \begin{cases} \mathbf{B}_K({}^i\tilde{\boldsymbol{\Phi}}_{AK}) & \text{if K is a transition node} \\ \mathbf{B}_K({}^i\boldsymbol{\Phi}) & \text{if K is a regular node} \end{cases} \\ \mathbf{B}_{BK} &= \mathbf{B}_K({}^i\tilde{\boldsymbol{\Phi}}_{BK}) \quad \text{if K is a transition node} \,. \end{aligned} \tag{32}$$

which leads to

$$\mathbf{B}_L = [\mathbf{B}_{L1}, \mathbf{B}_{L2}, \mathbf{B}_{L3}, \mathbf{B}_{L4}] \qquad (L = A, B) \,. \tag{33}$$

Then the FE–equation of element e yields

$$\begin{bmatrix} \mathbf{K}_{AA} & \mathbf{K}_{AB} \\ \mathbf{K}_{BA} & \mathbf{K}_{BB} \end{bmatrix} \begin{bmatrix} \Delta\mathbf{v}_A \\ \Delta\mathbf{v}_B \end{bmatrix} = \begin{bmatrix} \mathbf{R}_A \\ \mathbf{R}_B \end{bmatrix} \tag{34}$$

with

$$
\begin{aligned}
\mathbf{K}_{LM} &= \int_{(\Omega_e)} \sum_{j=1}^{n} \int_{(\Theta^3)} (\mathbf{B}_L^T \, {}^j\mathbf{C} \, \mathbf{B}_M + {}^j\mathbf{G}_{LM}) \, J \frac{{}^j h}{2} d^j\zeta \, d\Omega_e \\
\mathbf{R}_L &= \mathbf{P}_L - \int_{(\Omega_e)} \sum_{j=1}^{n} \int_{(\Theta^3)} \mathbf{B}_L^T \, \mathbf{S} \, J \frac{{}^j h}{2} d^j\zeta \, d\Omega_e \\
\Delta\mathbf{v}_L &= [\Delta\mathbf{v}_{1L}, \Delta\mathbf{v}_{2L}, \Delta\mathbf{v}_{3L}, \Delta\mathbf{v}_{4L}] \\
\Delta\mathbf{v}_{AK} &= \begin{cases} [\Delta\mathbf{u}_0, \Delta\boldsymbol{\beta}]_K & \text{if K is a transition node} \\ \Delta\mathbf{v}_K & \text{if K is a regular node} \end{cases} \\
\Delta\mathbf{v}_{BK} &= [\Delta^1\mu, \cdots, \Delta^i\mu, \cdots, \Delta^N\mu]_K \qquad \text{if K is a transition node}
\end{aligned}
\tag{35}
$$

where $L, M = A, B$ and ${}^j\mathbf{G}_{LM} = {}^j\mathbf{G}(\tilde{\boldsymbol{\Phi}}_L, \tilde{\boldsymbol{\Phi}}_M)$. The load vector $\mathbf{P}_L$ has to be computed as in a standard element considering (21).

The number of unknowns at the transition nodes is now $ndf = 5 + N$. In the following the N nodal unknowns which are strains of N numerical layers are condensed out. Provided $\mathbf{K}_{BB}$ is invertible the condensation leads to modified stiffness and right hand side

$$
\begin{aligned}
\tilde{\mathbf{K}}_{AA} &= \mathbf{K}_{AA} - \mathbf{K}_{AB}\mathbf{K}_{BB}^{-1}\mathbf{K}_{BA} \\
\tilde{\mathbf{R}}_A &= \mathbf{R}_A - \mathbf{K}_{AB}\mathbf{K}_{BB}^{-1}\mathbf{R}_B \, .
\end{aligned}
\tag{36}
$$

Within the Newton iteration the update of the condensed vector $\mathbf{v}_B$ yields

$$
\mathbf{v}_B^{l+1} = \mathbf{v}_B^l + \Delta\mathbf{v}_B \, . \tag{37}
$$

Hence the vector $\mathbf{v}_B^l$ has to be stored for each transition element.

Remark:

The condensation of $\mathbf{v}_B$ in (34) is not necessary, however it keeps the number of unknowns at the transition nodes with $ndf = 5$ the same as for the nodes within the 2D–domain. Thus the input data for the mesh generation becomes simple.

5 Numerical Examples

The element scheme has been implemented in an enhanced version of the program FEAP documented in ref. [42]. In this section we present three numerical examples to show the effectiveness of the finite element formulation presented above. The first example demonstrates the application of our formulation to a linear problem with the typical edge effect for laminated structures. Within the second and third example, a composite leaf spring and a plate with delamination, different finite elements are used in nonlinear applications.

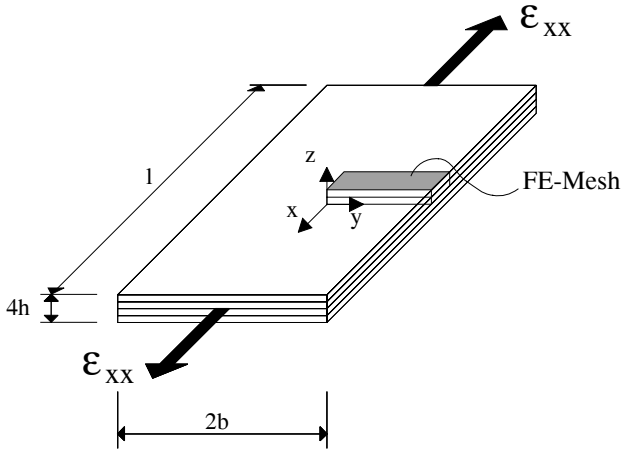

Figure 5: Rectangular plate under uniform uniaxial extension

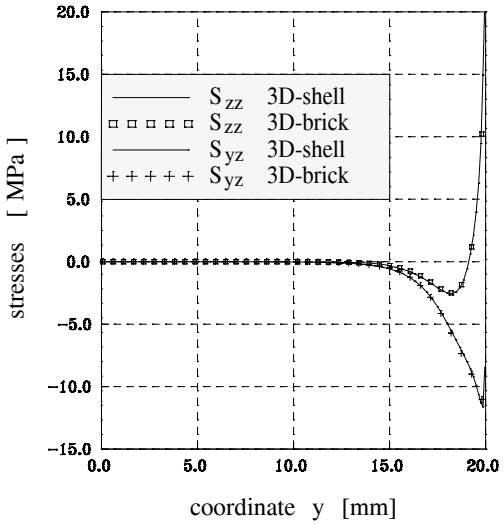

Figure 6: Comparison of the multi–director element with an 8–node brick element for the rectangular plate

5.1 Rectangular Plate under Uniform Uniaxial Extension

This well–known problem, presented in Fig. 5, is examined as first example, see e.g. ref. [35]. The laminate considered in this study consists of four identical plies with [0°/90°/90°/0°] stacking sequence where 0° refers to the x–direction. The width to height ratio is $b/h = 20$, where $h = 1$ represents one layer thickness and b half–width of the plate. The elastic constants with respect to principal material axes are:

$$\begin{aligned} E_1 &= 137900\,MPa, \qquad E_2 = 14480\,MPa, \\ \nu &= 0.25\,, \qquad G_{12} = G_{23} = 5860\,MPa\,. \end{aligned} \tag{38}$$

The strain state is constant in x–direction with $\varepsilon_{xx} = 10^{-2}$, thus one element is sufficient in this direction. Considering symmetry the upper two layers and half the system in y–direction is modeled with 100 elements. This example shows the typical edge effect for

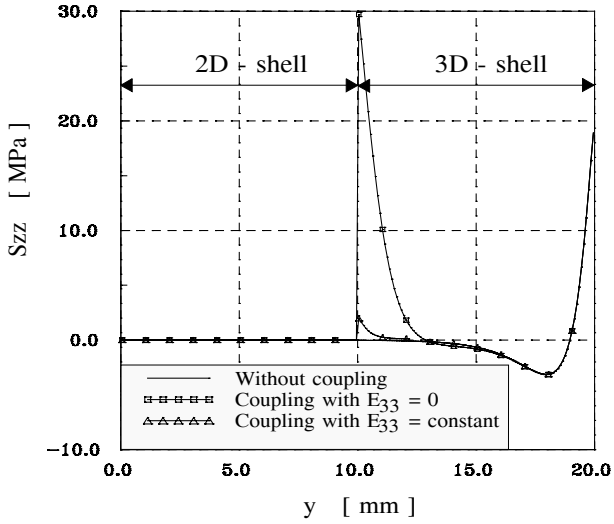

Figure 7: Stress distribution $S_{zz}(y, z = 0.1)$ for inappropriate transition conditions

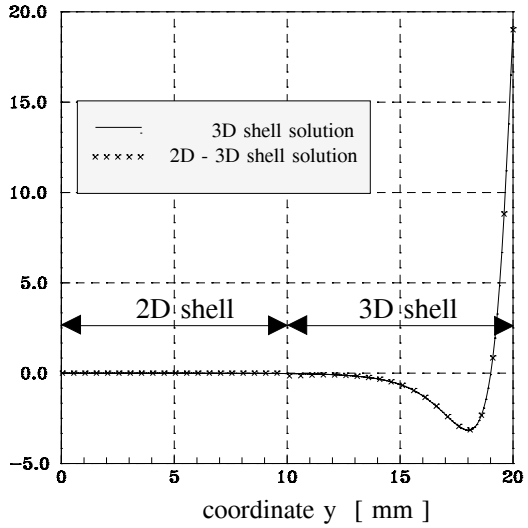

Figure 8: Shape of the normal stresses $S_{zz}(y, z = 0.1)[MPa]$

laminates. The stresses S_{zz} and S_{yz} are computed and compared with results obtained with 8–node brick elements. According to Fig. 6 there is good aggreement between both solutions. The developed FE–formulation is able to represent the steep ascent of the stress field along the free edges. Furthermore the plot shows that approximately plane stress state is given for $y < 10$. Thus in the next computation we discretize only the domain $10 \leq y \leq 20$ with 3d–shell elements and the remaining part with 5–parameter shell elements. Fig. 7 shows the results for two inappropriate transition conditions:
$E_{33}(y = 10, z) = 0, E_{33}(y = 10, z) = constant$. This example shows clearly that especially the assumption of inextensibility yields a completely wrong stress field in the vicinity of the transition elements. The results for the developed transition element with layerwise constant thickness stretches are depicted in Fig. 8 (S_{zz}) and Fig. 9 (S_{yz}). As can be seen there is good agreement between the 2D/3D and the 3D shell solution.

The shapes of the normal stress $S_{zz}(y = 19.95)$ through the thickness for two different discretizations are depicted in Fig. 10. A comparison for 20 numerical layers with linear interpolation and 4 layers with cubic interpolation is given. The zero stress condition at the top and bottom surfaces of the laminate is approximately fulfilled by the weak form of equilibrium.

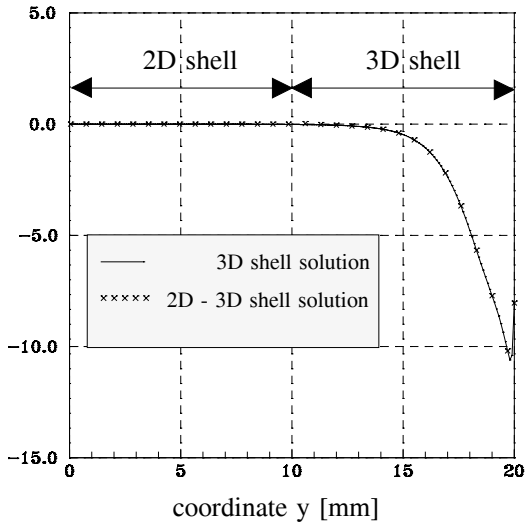

Figure 9: Shape of the shear stresses $S_{yz}(y, z = 1.1)[MPa]$

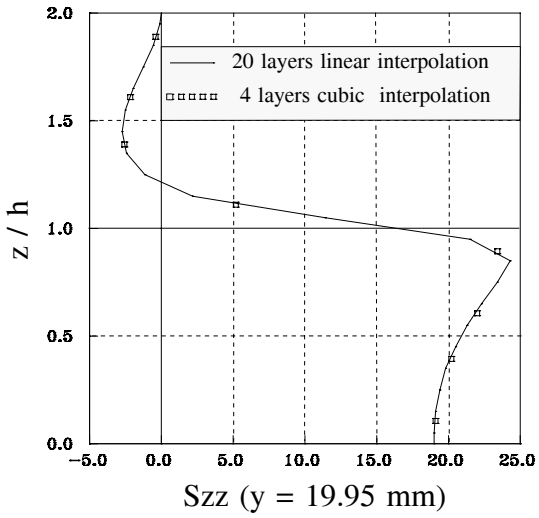

Figure 10: Distribution of normal stresses $S_{zz}(y = 19.95, z)[MPa]$ through the thickness

5.2 Composite Leaf Spring

The edge effect for a bending problem is investigated with the leaf spring shown in Fig. 11. The geometry of the spring is described by the parabola $z = 0.1\,x^2$. Additional data

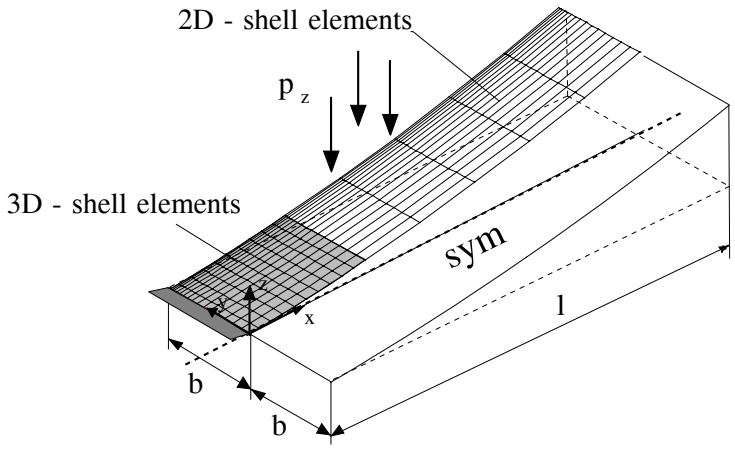

Figure 11: Leaf spring, geometry and loading

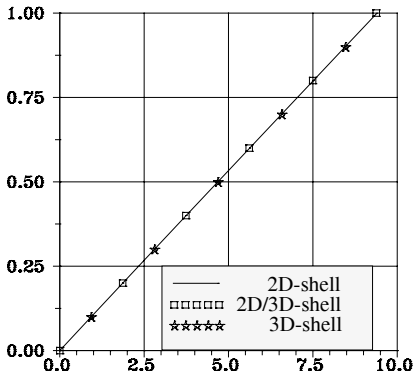

Figure 12: Load factor versus tip deflection of the leaf spring

are the total thickness with $h = 2$, a stacking sequence $[0°/90°/90°/0°]$, the length $l = 100$ and half–width $b = 20$. Material data are given in eq. (38). Due to the symmetry half of the system is discretized by 225 4–node elements. Each layer is subdivided into three sublayers with linear interpolation of the displacements in thickness direction. The mesh is refined along the free edge to catch the edge effects. The load deflection curve is computed up to a maximum load of $q_z = -6 \cdot 10^{-2}\, MPa$ for three different types of discretization: 5–parameter shell for the whole mesh, partly 3D–shell according to Fig. 11 and 3D–shell for the whole mesh. Fig. 12 shows that the results agree with each other. The computing times for a linear solution and different types of discretization on an IBM RS 6000–32H are given in Table 1. A considerable save of computing time is possible when using the developed coupling method. Furthermore a plot of the shear stresses $S^{23}(\Theta^3 = -0.417)$ shows the typical edge effect, see Fig. 13.

Next the thickness of the leaf spring is reduced to $h = 0.2$ to demonstrate the shear locking effect. The other geometrical and material data are unchanged. The results for a load $q_z = -6 \cdot 10^{-5}\, MPa$ are depicted in Fig. 14. Within a linear analysis the tip deflections of the spring are computed using the following discretizations: 3D–shell for the whole mesh, 2D–shell coupled with 3D–shell and 8–node brick elements based on the displacement method. The plot shows that the 8–node brick element suffers from severe

Discretization	CPU time [sec]
2D–shell	4.2
2D–3D–shell	214
3D–shell	445

Table 1: CPU–time for leaf spring

shear locking whereas the layered shell formulation yields already converged solutions for very course meshes. Especially this example shows the necessity of the developed layered shell formulation. An element based on a first–order shear deformation theory is not able to represent the correct shape of the edge stresses. On the other hand a discretization with brick elements leads especially for bending problems not to reliable results.

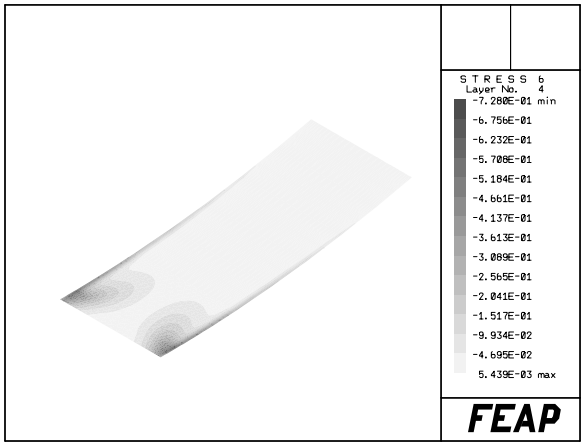

Figure 13: Contours of the shear stresses $S^{23}(\Theta^3 = -0.417)$

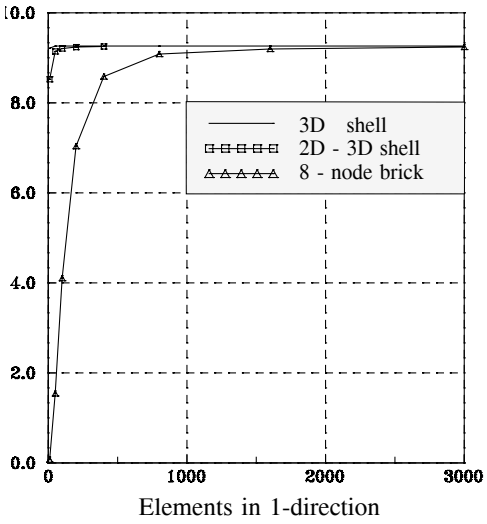

Figure 14: Tip deflection of the thin leaf spring for different elements

5.3 Stability Analysis of a Cracked Plate

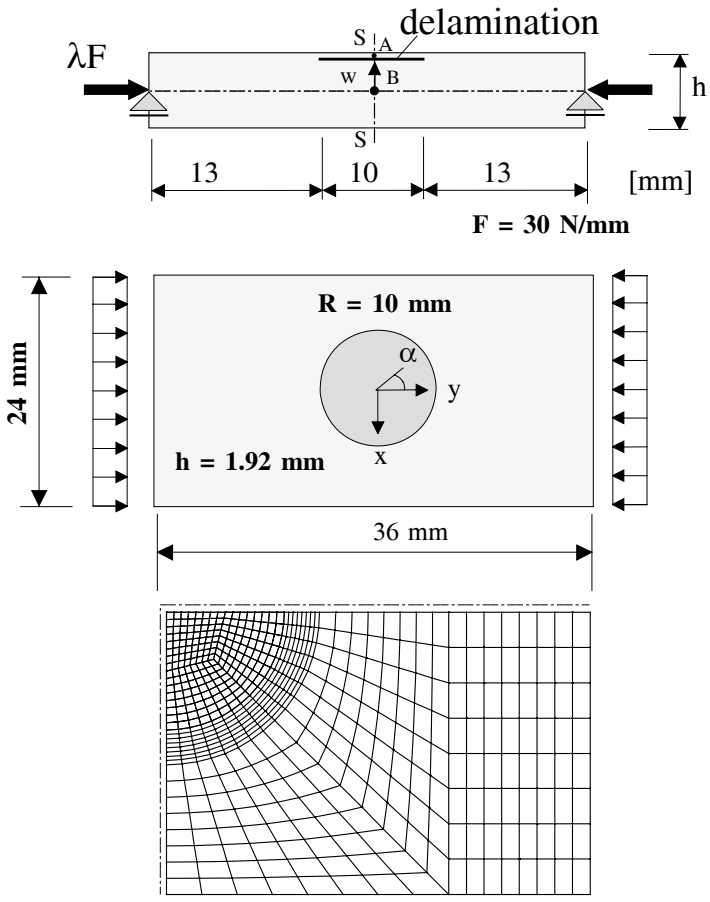

Figure 15: Cracked plate with a circular delamination zone

Within the last example the postcritical behaviour of a rectangular plate with a given circular delamination zone under pressure load is investigated, see Fig. 15. For this example results with nonlinear DKT–shell elements are published recently by Cochelin et.al. [33]. The plate consists of 16 layers with a $[0°/0°/+45°/0°/0°/-45°/0°/90°]_s$ stacking sequence. The artificial delamination zone is assumed between layer 14 and 15. Due to the symmetry only one quarter of the system is discretized with 704 4–node shell elements where we discretize the delamination zone with elements for the lower and upper part. The symmetry conditions are applied at $x = 0$ and $y = 0$ and $u_z = 0$ at the remaining boundaries. The displacements $u_y(y = 18\ mm)$ are constant which means that the load is applied via a rigid plate. Geometrical and material data are

$$\begin{aligned} l &= 36\,mm \\ b &= 24\,mm \\ t &= 0.12\,mm \\ h &= 1.92\,mm \end{aligned} \qquad \begin{aligned} E_1 &= 135000 \quad MPa \\ E_2 &= 8500 \quad MPa \\ \nu &= 0.317 \\ G_{12} &= 5150 \quad MPa \\ G_{23} &= 5150 \quad MPa\,. \end{aligned} \tag{39}$$

In a first step we use a classical shear elastic shallow shell element for composite material, see e.g. a modified element of Wagner et.al. [38], to verify the results of Cochelin et.al. [33].

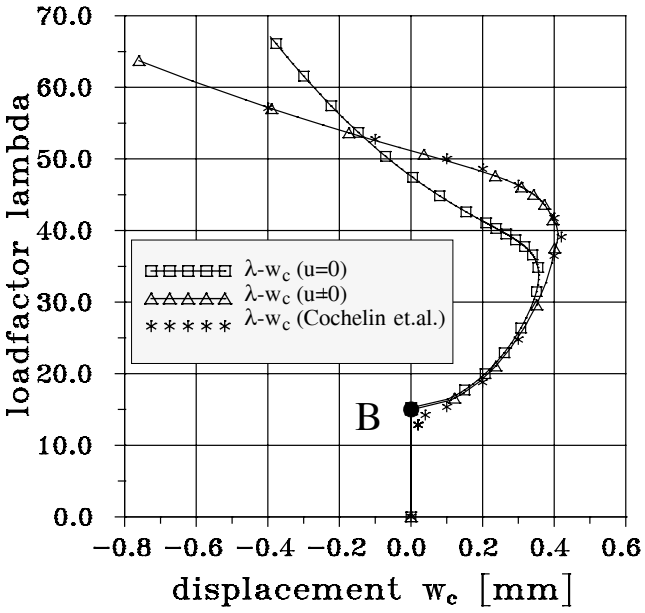

Figure 16: Load deflection curves for point A

The shallow shell element and the nonlinear version of the DKT–element, see Cochelin et.al. [34], are characterized by the same type of nonlinearity. The load factor λ versus the transverse displacement of point A in the center is depicted in Fig. 16 for two types of boundary conditions. The results for $u_x(x = 12) \neq 0$ are nearly similar to those of Cochelin et.al. [33] whereas we get a a different solution for boundary condition $u_x(x = 12) = 0$.

Our calculations base on the arc-length-method in combination with the use of so called extended systems for the stability analysis. We start with one arc-length step to find a solution point near the first stability point. This point - a bifurcation point - can be found directly within a given accuracy using the mentioned extended system at a load factor $\lambda = 14.98$. The associated lowest eigenvector is characterized by local buckling of the delaminated layers 15 and 16. A switch to the secondary path is possible by a perturbation of the primary solution with the first eigenvector. A detailed description of the used path following strategies in combination with extended systems can be found e.g. in Wagner, Wriggers [39] and Wriggers, Wagner, Miehe [41]. We get the ideal solution path in the prebuckling– and initial postbuckling range which is in contrast to Cochelin et.al. where imperfections are used to avoid the bifurcation analysis. The secondary equilibrium path is a stable solution path. Due to the buckled layers 15 and 16 the plate is now loaded excentrically which can be seen as an imperfection.

In Fig. 17 we present curves for the loadfactor λ versus the transverse displacement of points A and B in the center. Furthermore we make a calculation without a delamination zone. For this purpose we tie the nodes of top and bottom shell. The buckling load factor is now $\lambda_c = 50.93$. This point (B_2) and the associated secondary path are depicted in Fig. 17 too. It can be seen that the result with the delamination zone approaches this solution in the postcritical range. A simple analytical calculation for the buckling load of an orthotropic (here only approximately fulfilled) simply supported plate under

compression load leads to a critical load factor

$$\lambda_{cr} = \frac{2\,\pi^2}{F\,b^2}(\sqrt{D_{11} + D_{22}} + (D_{12} + 2D_{33})\,) = 47.6 \tag{40}$$

with $b = 24\,mm$, $F = 30\,N/m$ and D_{ii} the bending stiffness in directions 1,2 and 3=12, see e.g. Calcote [32].

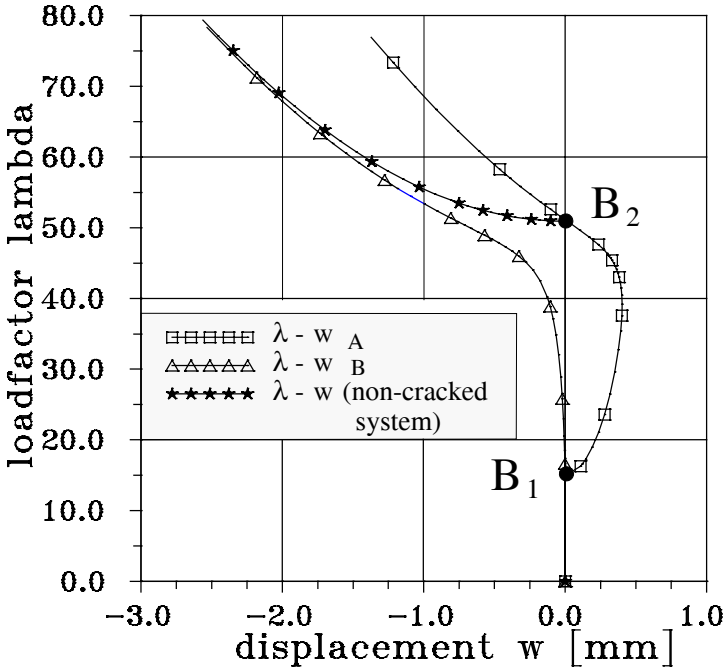

Figure 17: Load deflection curves for points A and B

In a second step we use a shear elastic shell element for composite materials including finite rotations, see e.g. Wagner, Gruttmann [40]. Here we get different results for the load deflection curves. Especially the bifurcation is now at $\lambda_c = 20.79$ which is about 39 % higher than with the shallow shell element. This is explained with the different types of shell formulation. The finite rotation element considers all nonlinear terms in the strain–displacement relations whereas the shallow shell element bases on a simplified moderate rotation theory with nonlinear terms only in $w_{,x}$ and $w_{,y}$. Without delamination we have a buckling load of $\lambda = 50.0$ which is about 1.8 % lower than with the shallow shell element. The complete load–deflection curve is shown in Fig. 18 together with the previous results from Fig. 16.

In a third step we test the above presented 3D–shell and the transition element. A ring of 3D–shell elements around the crack tip as depicted in Fig. 19 is used. This is to describe the three–dimensional stress state in the vicinity of the crack tip. The load–deflection relation agrees with the solution of the finite rotation element with 5 degrees of freedom as depicted in Fig. 18. A contour plot of stresses S_{zz} is given in Fig. 20. Further investigations e.g. the calculation of energy release rates as criteria for crack propagation could base on these results. Finally the deformed system at a load factor $\lambda = 60$ is plotted in Fig. 21. Global and local buckling deformations can be seen clearly.

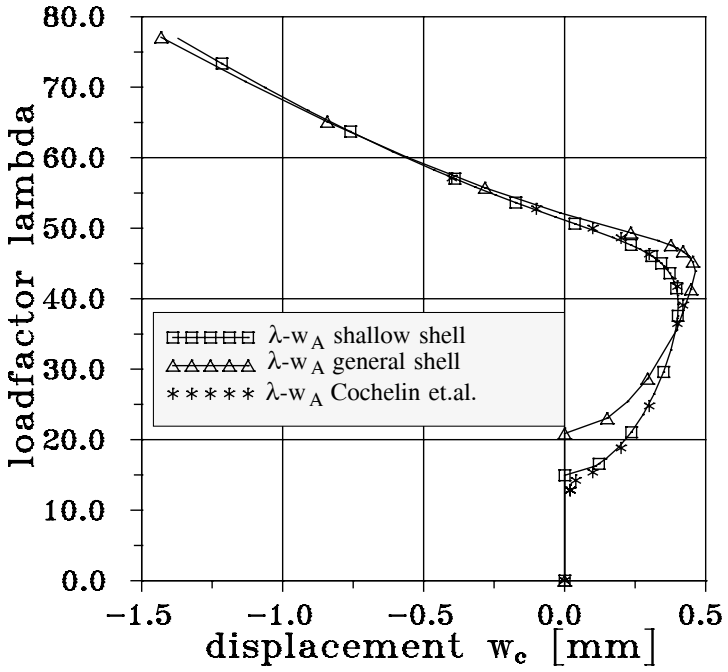

Figure 18: Load deflection curves for point A, comparison of a shallow shell element with a general shell element

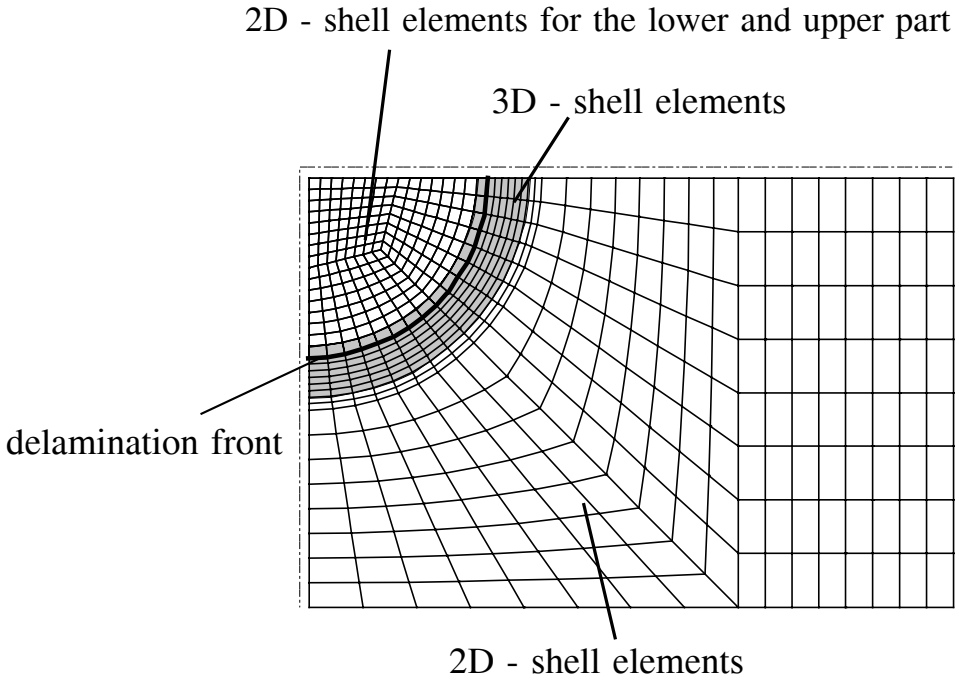

Figure 19: FE–mesh with distribution of 2D–shell and 3D–shell elements

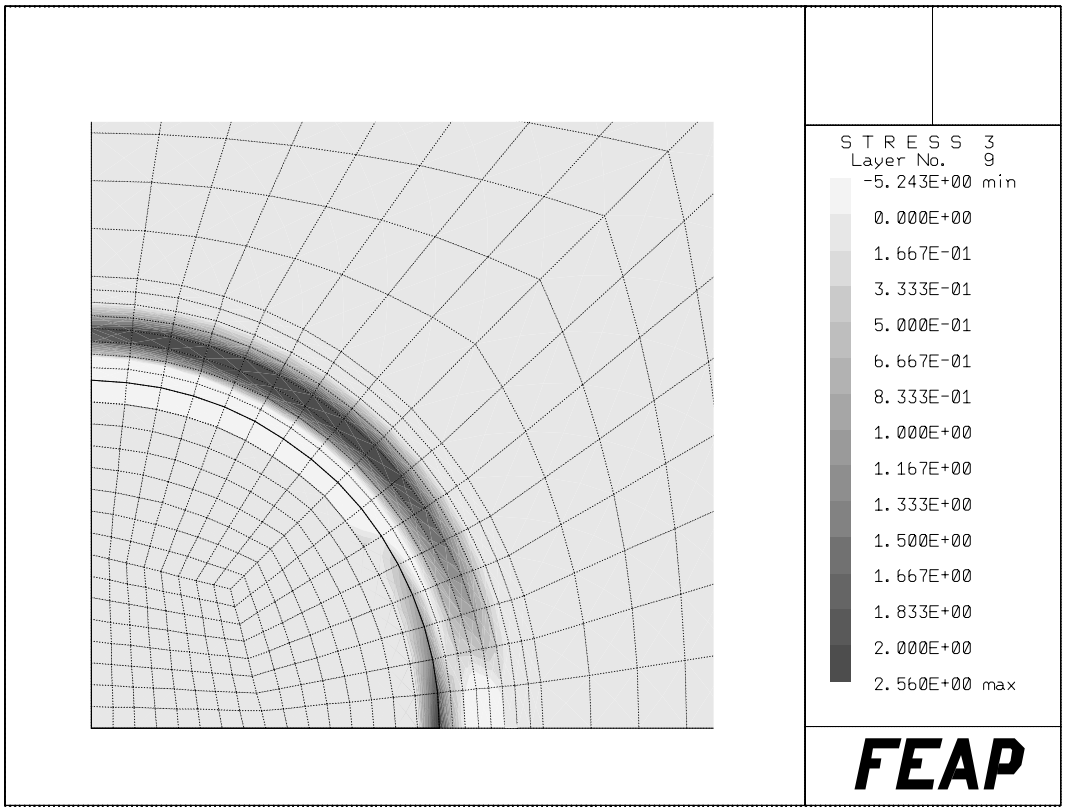

Figure 20: Contour plot of stresses S_{zz}

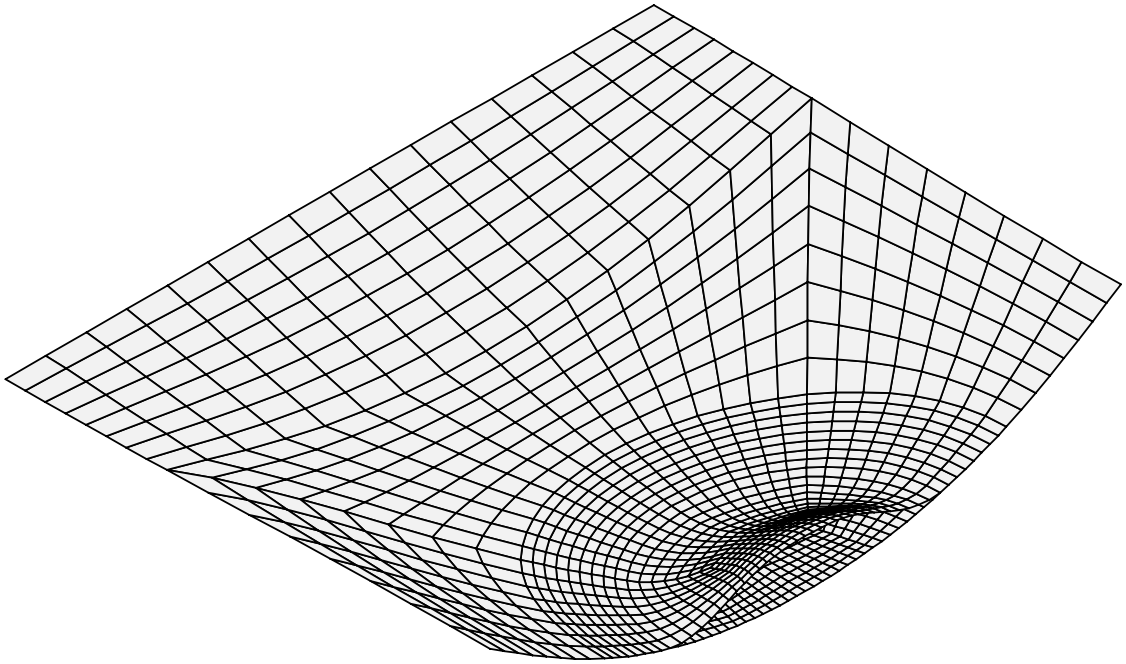

Figure 21: Deformed delaminated plate at $\lambda = 60$

6 Concluding Remarks

In this paper a geometrical nonlinear theory for the numerical analysis of composite structures is described. The kinematic is based on the assumption of independent interpolation functions for the displacement field through the thickness. The finite element formulation for quadrilaterals is based on the isoparametric approach. Initial geometry and displacement field are interpolated using bilinear functions. The transverse shear strains are independently approximated to avoid shear locking. Exact linearization of the variational equations yields tangential stiffness matrices used in the iterative solution process.

The developed model is characterized by the following features which provides several advantages compared to a FE–discretization with brick elements. The advantages are: 2–D data structure, simplified mesh generation, faster stiffness computation, better description of bending behaviour and a simple coupling of the developed element with standard shell elements.

The model is capable to describe edge effects emanating from the anisotropic material behaviour which are responsible for delamination phenomena. The results of different models are compared and show good agreement.

7 Appendix

A1 FE–matrices of the virtual strains

In this appendix we present the finite element matrices of the variational equations. We need to specify the variation of the Green–Lagrangian strain tensor $\delta\mathbf{E} = \delta\mathbf{F}^T\mathbf{F} + \mathbf{F}^T\delta\mathbf{F}$. Considering interpolation (18) the discrete form of the virtual deformation gradient leads to

$$\begin{aligned} \delta\mathbf{F} &= \delta\mathbf{x}_{,\alpha} \otimes \mathbf{e}_\alpha + \delta\mathbf{x}_{,3} \otimes \mathbf{e}_3 \\ \delta\mathbf{x}_{,\alpha} &= \sum_{K=1}^{4} N_{K,\alpha}\, \mathbf{\Phi}\, \delta\mathbf{v}_K \qquad \delta\mathbf{x}_{,3} = \sum_{K=1}^{4} N_K \mathbf{\Phi}_{,3}\ \delta\mathbf{v}_K \end{aligned} \tag{41}$$

This is inserted into the expression for the virtual strains $(7)_2$ $\delta\mathbf{E} = [\delta E_{11}\,, \delta E_{22}\,, \delta E_{33}\,, 2\delta E_{12}\,, 2\delta E_{13}\,, 2\delta E_{23}]^T$

$$\delta\mathbf{E} = \sum_{K=1}^{nel} \mathbf{B}_K \delta\mathbf{v}_K \qquad \mathbf{B}_K = \begin{bmatrix} \mathbf{B}_M \\ \\ \mathbf{J}^{-1}\mathbf{B}_S \end{bmatrix} \tag{42}$$

where

$$\mathbf{B}_M = \begin{bmatrix} N_{K,1}\, \mathbf{x}^T{}_{,1}\, \mathbf{\Phi} \\ N_{K,2}\, \mathbf{x}^T{}_{,2}\, \mathbf{\Phi} \\ N_K \mathbf{x}^T{}_{,3}\, \mathbf{\Phi}_{,3} \\ (N_{K,1}\, \mathbf{x}^T{}_{,2} + N_{K,2}\, \mathbf{x}^T{}_{,1})\mathbf{\Phi} \end{bmatrix} \qquad \mathbf{B}_S = \begin{bmatrix} N_{K,\xi}\, (\mathbf{x}_{M,3}^T\, \mathbf{\Phi} + f_M \mathbf{x}_{M,\xi}^T\, \mathbf{\Phi}_{,3}\,) \\ N_{K,\eta}\, (\mathbf{x}_{L,3}^T\, \mathbf{\Phi} + f_L \mathbf{x}_{L,\eta}^T\, \mathbf{\Phi}_{,3}\,) \end{bmatrix} \tag{43}$$

The variation of the assumed transverse shear interpolation (19) leads after some algebraic manipulations to matrix $\mathbf{B}_S$. The factors f_M and f_L with subscripts M, L are given in Table 2. Furthermore transformation of the shear strains into the orthogonal basis system is considered in (42).

K	1	2	3	4
M	B	B	D	D
L	A	C	C	A
f_M	-1	1	1	-1
f_L	-1	-1	1	1

Table 2: Nodes M and L for transverse shear interpolation

A2 Geometrical part of the tangential stiffness matrix

Numerical effectivity of the iterative solution procedure relies essentially on the correct linearization of the weak form of equilibrium. This leads to a material and a geometrical part within the tangential stiffness matrix. The geometrical part is deduced from (9) where we omit the layer index j

$$\mathbf{G}_{KL} = \widehat{N}_{KL}\boldsymbol{\Phi}^T\boldsymbol{\Phi} + S^{33}N_K N_L \boldsymbol{\Phi}^T{}_{,3}\,\boldsymbol{\Phi}_{,3} + \widehat{Q}_{KL}\boldsymbol{\Phi}^T{}_{,3}\,\boldsymbol{\Phi} + \widehat{Q}_{LK}\boldsymbol{\Phi}^T\boldsymbol{\Phi}_{,3} \tag{44}$$

with

$$\widehat{N}_{KL} = \tfrac{1}{2}S^{\alpha\beta}(N_{K,\alpha}\,N_{L,\beta} + N_{K,\beta}\,N_{L,\alpha}\,)$$

$$[\widehat{Q}_{KL}] = \frac{1}{8}\begin{bmatrix} -S^{\xi 3}(1-\eta) \\ -S^{\eta 3}(1-\xi) & -S^{\xi 3}(1-\eta) & 0 & -S^{\eta 3}(1-\xi) \\ S^{\xi 3}(1-\eta) & \begin{matrix} S^{\xi 3}(1-\eta) \\ -S^{\eta 3}(1+\xi) \end{matrix} & -S^{\eta 3}(1+\xi) & 0 \\ 0 & S^{\eta 3}(1+\xi) & \begin{matrix} S^{\xi 3}(1+\eta) \\ +S^{\eta 3}(1+\xi) \end{matrix} & S^{\xi 3}(1+\eta) \\ S^{\eta 3}(1-\xi) & 0 & -S^{\xi 3}(1+\eta) & \begin{matrix} -S^{\xi 3}(1+\eta) \\ +S^{\eta 3}(1-\xi) \end{matrix} \end{bmatrix} \tag{45}$$

$$\widehat{Q}_{LK} = -\widehat{Q}_{KL}\,.$$

Here it is more convenient to express the transverse shear part in the skew basis system. The transformed shear stresses are

$$\begin{bmatrix} S^{\xi 3} \\ S^{\eta 3} \end{bmatrix} = \mathbf{J}^{-1} \begin{bmatrix} S^{13} \\ S^{23} \end{bmatrix}. \tag{46}$$

Acknowledgment
The financial support of the Deutsche Forschungsgemeinschaft (DFG) is gratefully acknowledged.

8 References

1. Kapania R. K., Raciti S., Recent advances in analysis of laminated beams and plates, part I: Shear effects and buckling, *AIAAJ.*, **27** (1989) 923–934.

2. Noor A. K., Burton W. S., Peters J. M., Assessment of computational models for multilayered composite cylinders, in: A.K. Noor et al.(eds), Analytical and Computational Models of Shells, Vol.3, ASME, New York, 419–441, (1989) .

3. Whitney J. M., Pagano N. J., Shear deformation in heterogeneous anisotropic plates, *J. Appl. Mech. ASME*, **37** (1970) 1031–1036.

4. Klarmann R., Nichtlineare Finite Element Berechnungen von Schalentragwerken mit geschichtetem anisotropen Querschnitt, Heft 12 der Schriftenreihe des Instituts fr Baustatik der Universität Karlsruhe, (1991).

5. Reddy J. N., A simple higher theory for laminated composite plates, *J. Appl. Mech. ASME*, **51** (1984) 745–752.

6. Lee C., Liu D., An Interlaminar Stress Continuity Theory for Laminated Composite Analysis, *Comp. & Struct.*, **42** (1992) 69–78.

7. Pagano N. J., Exact Solutions for rectangular bidirectional composites and sandwich plates, *J. Comp. Mat.* **4** (1970) 20–34.

8. Epstein M., Huttelmaier H. P., A Finite Element Formulation for Multilayered and Thick Plates, *Comp. & Struct.*, **5** (1983) 645–650.

9. Toledano A., Murakami H., A High–Order Laminated Plate Theory with Improved In–plane Responses, *Int. J. Solids Structures*, **23** (1987) 111–131.

10. Reddy J. N., Barbero E. J., Teply J. L., A Plate Bending Element Based on a Generalized Laminate Plate Theory, *Int. J. Num. Meth. Engng.*, **28** (1989) 2275–2292.

11. Li Z. H., Owen D. R. J., Elastic–Plastic Analysis of Laminated Anisotropic Shells by a Refined Finite Element Laminated Model, *Comp. & Struct.*, **32** (1989) 361–382.

12. Tessler A., Saether E., A Computationally Viable Higher–Order Theory for Laminated Composite Plates, *Int. J. Num. Meth. Engng.*, **31** (1991) 1069–1086.

13. Puchta N. S., Reddy J. N., A Mixed Shear Flexible Element for the Analysis of Laminated Plates, *Comp. Meth. Appl. Mech. Engng.*, **44** (1984) 213–227.

14. Pinsky P., Jasti R. V., A Mixed Finite Element for Laminated Composite Plates based on the Use of Bubble Functions, *Eng. Comp.*, **6** (1989) 316–330.

15. Peseux B., Dubigeon S.: Equivalent Homogeneous Finite Element For Composite Materials Via Reissner Principle. Part II: Finite Element For Shells, *Int. J. Num. Meth. Engng.*, **31** (1991), 1497–1509.

16. Babuška I., Szabó B. A., Actis R. L., Hierarchic Models for Laminated Composites, *Int. J. Num. Meth. Engng.*, **33**, (1992) 503–535.

17. Robbins D.H., Reddy J. N., Modeling of Thick Composites Using a Layerwise Laminate Theory, *Int. J. Num. Meth. Engng.*, **36** (1993) 655–677.

18. Argyris, J., Tenek, L., Linear and Geometrically Nonlinear Bending of Isotropic and Multilayered Composite Plates by the Natural Mode Method, *Comp. Meth. Appl. Mech. Engng.*, **113** (1994) 207–251.

19. Argyris, J., Tenek, L., Buckling of Multilayered Composite Plates By Natural Shear Deformation Matrix Theory, *Comp. Meth. Appl. Mech. Engng.*, **111** (1994) 37–59.

20. Stanley, G. M., Park, K.C., Hughes, T.J.R., Continuum–based resultant shell elements, *Finite Element methods for Plate and Shell Structures* (Eds. Hughes, T.J.R., Hinton, E.) Pineridge Press, Swansea, (1986) 1–45.

21. Reddy J. N., Chandrashekhara K., Nonlinear Analysis of Laminated Shells Including Transverse Shear Strains, *AIAA Journal*, **23** (1985) 440–441.

22. Wagner W., Gruttmann F., On the Stability Behaviour of Composite Shells, in: P. Ladevèze, O.C. Zienkiewicz (eds.) Proceedings of the European Conference on New Advances in Computational Structural Mechanics, Giens (France), (1991), 539–546.

23. Dorninger K., Rammerstorfer F., A Layered Composite Shell Element For Elastic and Thermoelastic Stress and Stability Analysis at Large Deformations, *Int. J. Num. Meth. Engng.*, **30** (1990) 833–858.

24. Dorninger K., A Nonlinear Layered Shell Finite Element With Improved Transverse Shear Behavior, *Composites Engineering*, **1** (1991) 211–224.

25. Wagner W., Stein E., A New Finite Element Formulation for Cylindrical Shells of Composite Material, *Composites Engineering*, **3** (1993), 899–910.

26. Başar Y., Ding Y., Schultz R., Refined Shear–Deformation Models for Composite Laminates with Finite Rotations, *Int. J. Solids Struct.* **30** (1993) 2611–2638.

27. Başar Y., Montag, U., Ding Y., On an Isoparametric Finite–Element for Composite Laminates with Finite Rotations, *Comp. Mech.* **12** (1993) 329–348.

28. Di S., Ramm E., Optimally Constraint Hybrid Element for Laminated Shells Based on Higher–Order Theory, *Comp. Meth. Appl. Mech. Engng.*, **109** (1993) 359–376.

29. Gruttmann F., Wagner W., Meyer L., Wriggers P., A Nonlinear Composite Shell Element with Continuous Interlaminar Shear Stresses, *Computational Mechanics*, **13**, (1993) 175–188.

30. Gruttmann F., Wagner W., On the Numerical Analysis of Local Effects in Composite Structures, *Composite Structures* **29**, (1994) 1–12.

31. Braun M., Bischoff, M., Ramm E., Nonlinear Shell Formulations for Complete Three–Dimensional Constitutive Laws, *Computational Mechanics*. **15**, (1994) 1–18.

32. Calcote, L. R., The Analysis of Laminated Composite Structures, Van Nostrand, New York (1969)

33. Cochelin, B., Damil, N., Potier–Ferry, M., Asymptotic–Numerical Methods and Padé Approximants for Nonlinear–Elastic Structures, *Int. J. Num. Meth. Engng.*, **37** (1994) 1187–1213.

34. Cochelin, B., Potier–Ferry, M., A Numerical Model for Buckling and Growth of Delaminations in Composite Laminates, *Comp. Meth. Appl. Mech. Engng.*, **89** (1991) 361–380.

35. Shah C.G., Krishna Murty A.V., Analysis of Edge Delaminations in Laminates Through Combined Use of Quasi–Three–Dimensional, Eight–Noded, Two–Noded and Transition Elements, *Computers & Structures*, **39** (1991) 231–242.

36. Simo, J. C., Fox D. D., Rifai, M. S., On a Stress Resultant Geometrically Exact Shell Model, Part III: Computational Aspects of the Nonlinear Theory, Comp. Meth. Appl. Mech. Engng., **79** (1990) 21-70

37. Stein, E., Rust, W., Ohnimus, S., H–and D–adaptive FE Methods for Two–dimensional Structural Problems including Post–buckling of Shells, *Comp. Meth. Appl. Mech. Engng.*, **101** (1992) 315–354.

38. Wagner, W., Wriggers, P., Stein E.: A shear-elastic Shell Theory and Finite-Element-Postbuckling Analysis including Contact, Euromech 200, ed. J. Szabo, Matrafüred (1985), 381–404.

39. Wagner, W., Wriggers, P., A Simple Method for the Calculation of Postcritical Branches, *Engineering Computations*, **5** (1988) 103–109.

40. Wagner W., Gruttmann F., A Simple Finite Rotation Formulation for Composite Shell Elements, *Engineering Computations*, **11**, 2 (1994), 145–176.

41. Wriggers, P., Wagner, W., Miehe, C., A Quadratically Convergent Procedure for the Calculation of Stability Points in Finite Element Analysis, *Comp. Meth. Appl. Mech. Engng.*, **70** (1988) 329–347.

42. Zienkiewicz O. C., Taylor R. L., The Finite Element Method, 4th edition, Vol. 1, McGraw Hill, London, (1988).